

Circumventing volumetric locking in explicit material point methods: A simple, efficient, and general approach

Yidong Zhao^a, Chenfanfu Jiang^b, Jinhyun Choo^{a,*}

^a*Department of Civil and Environmental Engineering, KAIST, South Korea*

^b*Department of Mathematics, University of California, Los Angeles, United States*

Abstract

The material point method (MPM) is frequently used to simulate large deformations of nearly incompressible materials such as water, rubber, and undrained porous media. However, MPM solutions to nearly incompressible materials are susceptible to volumetric locking, that is, overly stiff behavior with erroneous strain and stress fields. While several approaches have been devised to mitigate volumetric locking in MPM, none of them lends itself to a straightforward application to standard explicit MPM formulations. In this work, we propose a locking-mitigation approach that features an unprecedented combination of simplicity, efficacy, and generality for a family of explicit MPM formulations. The approach combines the assumed deformation gradient ($\bar{\mathbf{F}}$) method with a volume-averaging operation built on standard particle–grid transfer schemes in MPM. Upon explicit time integration, this combination yields a new and simple algorithm for updating the deformation gradient, preserving all other MPM procedures. The proposed approach is thus easy to implement, low-cost, and compatible with the existing machinery in MPM. Through various types of nearly incompressible problems in solid and fluid mechanics, we verify that the proposed approach efficiently circumvents volumetric locking in explicit MPM, regardless of the basis functions and material types.

Keywords: Material point method, Volumetric locking, Incompressible materials, Assumed deformation gradient, Large deformation, Dynamics

1. Introduction

The material point method (MPM) [1] is a hybrid Lagrangian–Eulerian numerical technique for continuum mechanics simulation, whereby physical quantities are traced via material points, or “particles,” and the governing equation (in its weak form) is solved in a background grid. The particles and the grid exchange their information through projection operations which use basis

*Corresponding Author

Email address: jinhyun.choo@kaist.ac.kr (Jinhyun Choo)

(interpolation) functions associated with the grid. Remarkably, MPM shares many features with the finite element method (FEM)—the most popular numerical method in solid mechanics—while it is rooted in the fluid implicit particle (FLIP) method [2]—a particle-in-cell (PIC) method for fluid dynamics. For this reason, MPM has been commonly used for simulating large deformation in a wide variety of solids and fluids alike (*e.g.* [3–6]).

When modeling nearly incompressible materials (*e.g.* water, rubber, and undrained porous media), MPM solutions are susceptible to volumetric locking, that is, overly stiff behavior with erroneous strain and stress fields. Volumetric locking commonly arises in FEM and related methods when integration points pose excessive incompressibility constraints on the calculation of element stiffness. Unfortunately, MPM is inherently vulnerable to volumetric locking, because it typically uses a combination of low-order basis functions and a large number of integration (material) points per element. In the FEM literature, a number of approaches have been proposed for mitigating locking, relaxing the incompressibility constraints on element kinematics in different ways. Among them, only those compatible with finite deformation kinematics as well as movable integration points may be adapted to MPM.

Locking-mitigation approaches that have been adapted to MPM can be categorized into the following four types. The first type is mixed multi-field formulations. For example, Love and Sulsky [7] and Mast *et al.* [8] have used a three-field MPM formulation based on the Hu–Washizu variational principle, and Iaconeta *et al.* [9] have presented a two-field formulation with stabilization. The second type is operator splitting algorithms explored by Zhang *et al.* [10] and Kularathna and Soga [11], which are built on Chorin’s projection method for incompressible fluid dynamics [12]. The third type is the assumed deformation gradient ($\bar{\mathbf{F}}$) method [13]. Coombs and coworkers [14, 15] have developed implicit $\bar{\mathbf{F}}$ MPM formulations for quasi-static solid mechanics, and Moutsanidis *et al.* [16] have proposed a different way to calculate $\bar{\mathbf{F}}$ in explicit particle methods. The fourth one is the nonlinear $\bar{\mathbf{B}}$ method [17], which is a large-strain generalization of the $\bar{\mathbf{B}}$ method originally proposed by Hughes [18] for small-strain FEM, extended to MPM recently by Bisht *et al.* [19, 20]. It is noted that the $\bar{\mathbf{F}}$ and nonlinear $\bar{\mathbf{B}}$ methods are highly related in that both methods rely on reduced integration of the volumetric part of a deformation measure (but their specific procedures are not exactly the same). Very recently, Telikicherla and Moutsanidis [21] have proposed a projection technique for reduced integration in MPM with high-order basis functions, whereby an additional background grid with low-order basis functions is introduced.

Nevertheless, none of the existing locking-mitigation approaches lends itself to straightforward application to standard explicit MPM formulations. The mixed formulations and operator splitting algorithms require one to change the standard governing equations and time-stepping scheme, respectively, demanding significant cost for implementation and utilization. Extension of these methods to multiphysical problems (*e.g.* coupled deformation and flow) is also a challenging endeavor. Regarding the $\bar{\mathbf{F}}$ and $\bar{\mathbf{B}}$ methods, their current MPM versions are either restricted to

basis functions that are not associated with adjacent elements (undesirable due to cell-crossing errors), or require a non-trivial modification of basis functions if they are associated with adjacent elements. As such, it is not straightforward to apply the existing $\bar{\mathbf{F}}$ or $\bar{\mathbf{B}}$ method to MPM formulations with different MPM basis functions such as B-splines [22, 23].

In this work, we present a new approach that is unprecedentedly simple, efficient, and general for circumventing volumetric locking in a family of standard explicit MPM formulations. The key idea is to calculate the assumed deformation gradient, $\bar{\mathbf{F}}$, using standard particle–grid transfer schemes in MPM, instead of the element-wise averaging operation or multiple background grids used in the existing $\bar{\mathbf{F}}$ method for MPM. Combining this idea with the standard explicit time discretization in MPM, we arrive at a new and simple algorithm for updating the deformation gradient. The new algorithm neither changes any other parts of the existing MPM machinery nor introduces any additional parameter. Therefore, this approach can be utilized in a straightforward manner, regardless of the MPM basis functions and material types. We implement the proposed approach with two types of MPM basis functions, namely, GIMP’s basis functions and B-splines, and verify it with various types of nearly incompressible problems arising in solid and fluid mechanics.

2. Material point method formulation

This section recapitulates the standard MPM formulation for a continuum body undergoing large deformation. For more details of the formulation, the reader is referred to [24–26].

2.1. Problem statement

Consider a continuum body whose current configuration is denoted by $\Omega \in \mathbb{R}^{\text{dim}}$, where “dim” refers to the spatial dimension. The boundary of Ω is denoted by $\partial\Omega$, and it is decomposed into the displacement (Dirichlet) boundary $\partial_u\Omega$ and the traction (Neumann) boundary $\partial_t\Omega$ such that $\partial_u\Omega \cap \partial_t\Omega = \emptyset$ and $\overline{\partial_u\Omega} \cup \overline{\partial_t\Omega} = \partial\Omega$. The time domain is denoted by $\mathcal{T} := (0, T]$ with $T > 0$.

Finite deformation theory should be used to accurately describe nonlinear kinematics in large deformation. Let us denote by \mathbf{X} and \mathbf{x} the position vectors of a material point in the reference and current configurations, respectively. The displacement vector of the material point is then defined as $\mathbf{u} := \mathbf{x} - \mathbf{X}$. The velocity and acceleration vectors are given by $\mathbf{v} := \dot{\mathbf{u}}$ and $\mathbf{a} := \dot{\mathbf{v}} = \ddot{\mathbf{u}}$, where the dot denotes the material time derivative. The deformation gradient is defined as

$$\mathbf{F} := \frac{\partial \mathbf{x}}{\partial \mathbf{X}} = \mathbf{1} + \frac{\partial \mathbf{u}}{\partial \mathbf{X}}, \quad (1)$$

where $\mathbf{1}$ is the second-order identity tensor. The Jacobian is defined as

$$J := \det(\mathbf{F}) = \frac{dv}{dV}, \quad (2)$$

where dV and dv are the differential volumes in the reference and current configurations, respectively.

Balance of linear momentum provides the governing equation. Since the standard MPM is built on the updated Lagrangian approach, we write the momentum balance equation in the current configuration as

$$\nabla \cdot \boldsymbol{\sigma}(\mathbf{F}) + \rho \mathbf{g} = \rho \dot{\mathbf{v}} \quad \text{in } \Omega \times \mathcal{T}, \quad (3)$$

where $\nabla \cdot (\circ)$ denotes the divergence operator defined in the current configuration, $\boldsymbol{\sigma}$ is the Cauchy stress tensor, ρ is the mass density, and \mathbf{g} is the gravitational acceleration vector. To close the equation, a constitutive relation between $\boldsymbol{\sigma}$ and \mathbf{F} should be introduced. In this work, we will consider a range of commonly used constitutive relations to demonstrate the generality of the proposed method. For brevity, we omit the details of these constitutive relations, referring to textbooks on this subject (*e.g.* [27–29]).

The initial–boundary–value problem of interest can be stated as follows. Find \mathbf{u} that satisfies Eq. (3), subject to the initial condition of $\mathbf{u} = \mathbf{u}_0$ and boundary conditions

$$\mathbf{u} = \hat{\mathbf{u}} \quad \text{on } \partial_u \Omega \times \mathcal{T}, \quad (4)$$

$$\mathbf{n} \cdot \boldsymbol{\sigma} = \hat{\mathbf{t}} \quad \text{on } \partial_t \Omega \times \mathcal{T}, \quad (5)$$

where $\hat{\mathbf{u}}$ and $\hat{\mathbf{t}}$ are the boundary displacement and traction, respectively, and \mathbf{n} is the unit outward normal vector in the current configuration.

Through the standard weighted residual procedure, the variational form of the governing equation can be formulated as

$$\int_{\Omega} \boldsymbol{\eta} \cdot \rho \dot{\mathbf{v}} \, dV = - \int_{\Omega} \nabla^s \boldsymbol{\eta} : \boldsymbol{\sigma}(\mathbf{F}) \, dV + \int_{\Omega} \boldsymbol{\eta} \cdot \mathbf{g} \, dV + \int_{\partial_t \Omega} \boldsymbol{\eta} \cdot \hat{\mathbf{t}} \, dA, \quad (6)$$

where $\boldsymbol{\eta}$ denotes the variation of the displacement field, and ∇^s is the symmetric gradient operator defined in the current configuration.

2.2. Material point method discretization

For MPM discretization of the problem, we introduce a set of particles (material points) filling the domain and a background grid that accommodates the particles. We then update the solution from the previous time step (t^n) to the next time step (t^{n+1}) through the procedure illustrated in Fig. 1. The MPM procedure is described in the following. Hereafter, we shall use subscript $(\circ)_p$ to denote quantities related to particles and use subscript $(\circ)_i$ to denote quantities related to nodes. We shall also use superscripts $(\circ)^n$ and $(\circ)^{n+1}$ to denote quantities at t^n and t^{n+1} , respectively.

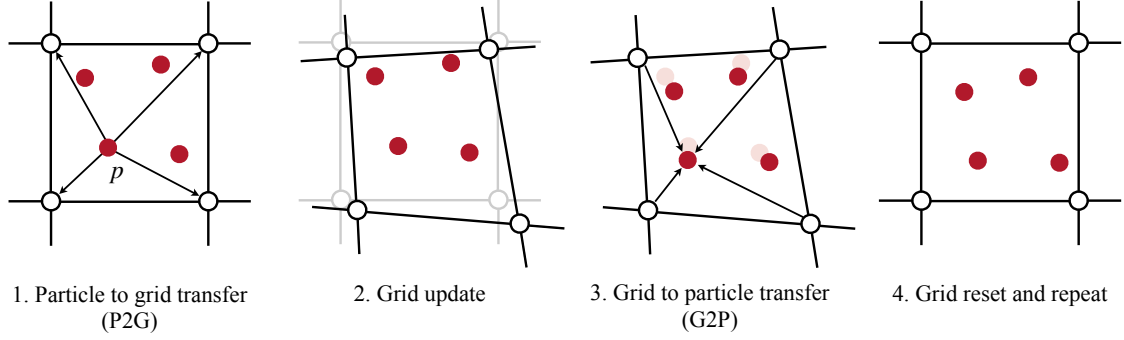


Figure 1: MPM update procedure.

Particle to grid transfer (P2G). First, we map the mass and momentum of each particle to nodes in the background grid. This process is called the particle-to-grid (P2G) transfer. The particle mass and momentum are transferred to the nodes as

$$m_i = \sum_p w_{ip} m_p, \quad (7)$$

$$m_i \mathbf{v}_i^n = \sum_p w_{ip} m_p \mathbf{v}_p^n, \quad (8)$$

where m_i and m_p are the nodal and particle masses, respectively, and \mathbf{v}_i and \mathbf{v}_p are the particle and nodal velocity vectors, respectively. Also, $w_{ip} := w_i(\mathbf{x}_p)$ is the basis function for interpolating values at node i to the position of particle p , and \sum_p is the summation over particles supported by the basis function associated with node i . In the MPM literature, a few types of basis functions have been employed. Among them, here we consider two popular choices, namely, (i) generalized interpolation material point (GIMP) [30] and (ii) B-splines [22]. Note that these basis functions are free of the cell-crossing error problem which may arise when the original MPM basis functions (linear shape functions) are used.

Grid update. Following the P2G transfer, we update the velocity vector at each node through the governing equation (6). As standard, we use the explicit Euler method to integrate the governing equation in time, and update the nodal velocity as

$$m_i \mathbf{v}_i^{n+1} = m_i \mathbf{v}_i^n + \Delta t (\mathbf{f}_i^{\text{int}} + \mathbf{f}_i^{\text{ext}}). \quad (9)$$

Here, $\Delta t := t^{n+1} - t^n$ is the time increment, and $\mathbf{f}_i^{\text{int}}$ and $\mathbf{f}_i^{\text{ext}}$ are the internal and external force vectors, respectively. The internal force vector is calculated as

$$\mathbf{f}_i^{\text{int}} = - \sum_p \nabla^s w_{ip} : \boldsymbol{\sigma}(\mathbf{F}_p) \mathbf{V}_p^n, \quad (10)$$

where V_p^n is the current particle volume. The external force vector is calculated from the body force and boundary traction vectors.

Grid to particle transfer (G2P). After updating the nodal velocity, we map it back to the particles and update the particle velocity. This procedure is called the grid-to-particle (G2P) transfer. Two schemes exist for updating the particle velocity: (i) the fluid-implicit-particle (FLIP) method [2] which transfers the velocity increment, and (ii) the particle-in-cell (PIC) method [31] which transfers the updated velocity itself. These two schemes can be written as

$$(\mathbf{v}_p^{n+1})_{\text{FLIP}} = \mathbf{v}_p^n + \sum_i w_{ip} (\mathbf{v}_i^{n+1} - \mathbf{v}_i^n), \quad (11)$$

$$(\mathbf{v}_p^{n+1})_{\text{PIC}} = \sum_i w_{ip} \mathbf{v}_i^{n+1}, \quad (12)$$

where \sum_i is the summation over nodes supporting particle p . While FLIP is less stable than PIC, it has significantly less numerical damping than PIC. In general, the FLIP and PIC schemes can be blended as

$$\mathbf{v}_p^{n+1} = \eta (\mathbf{v}_p^{n+1})_{\text{FLIP}} + (1 - \eta) (\mathbf{v}_p^{n+1})_{\text{PIC}}. \quad (13)$$

where $\eta \in [0, 1]$ is the blending coefficient. In this work, we shall use $\eta = 1$ by default. Subsequently, we update the deformation gradient, volume, stress, and position of each particle. The deformation gradient is updated as

$$\mathbf{F}_p^{n+1} = \left(\mathbf{1} + \Delta t \sum_i \mathbf{v}_i^{n+1} \otimes \nabla w_{ip} \right) \cdot \mathbf{F}_p^n. \quad (14)$$

The particle volume is updated as

$$V_p^{n+1} = J_p^{n+1} V_p^0, \quad (15)$$

where $J_p^{n+1} := \det \mathbf{F}_p^{n+1}$, and V_p^0 is the initial (reference) particle volume. For updating the stress tensor, we use the *relative* deformation gradient—analogueous to the incremental strain tensor in small-strain problems—to accommodate history-dependent material behavior. The relative deformation gradient is defined and calculated as

$$\Delta \mathbf{F}_p := \mathbf{F}_p^{n+1} \cdot (\mathbf{F}_p^n)^{-1} = \mathbf{1} + \Delta t \nabla \mathbf{v}_p^{n+1}. \quad (16)$$

By assigning the relative deformation gradient to the specific constitutive relation, the stress tensor is updated. Lastly, the particle position is updated as

$$\mathbf{x}_p^{n+1} = \mathbf{x}_p^n + \Delta t \sum_i w_{ip} \mathbf{v}_i^{n+1}. \quad (17)$$

Grid reset and repeat. After updating the state variables and positions of the particles, we reset the background grid, move to the next time step, and repeat the aforementioned procedure. It would be worthwhile to note that the grid is not reset in total Lagrangian MPM formulations (e.g. [32, 33]). Here, we focus on standard MPM formulations built on an updated Lagrangian approach.

3. Circumventing volumetric locking

In this section, we formulate a new approach to mitigating volumetric locking in MPM. We first adopt the assumed deformation gradient ($\bar{\mathbf{F}}$) method—originally proposed for overcoming volumetric locking in FEM [13]—in the context of MPM. We then present a new way to calculate the assumed deformation gradient in MPM, which averages the volumetric part of the deformation gradient (the Jacobian) through particle–grid transfer operations. Subsequently, we develop a detailed procedure to apply the proposed method in MPM.

3.1. Assumed deformation gradient method

The key idea of the assumed deformation gradient method is to replace the deformation gradient (\mathbf{F}) in the constitutive relation by an assumed deformation gradient ($\bar{\mathbf{F}}$), where the volumetric part of \mathbf{F} (i.e. the Jacobian, J) is volume-averaged in some manner. When applied to the current formulation, it replaces \mathbf{F}_p in the constitutive relation by

$$\bar{\mathbf{F}}_p = \left(\frac{\bar{J}_p}{J_p} \right)^{1/\dim} \mathbf{F}_p, \quad (18)$$

where \bar{J}_p denotes the averaged Jacobian, which is subject to fewer volumetric constraints than J_p . It can be seen that $(\bar{J}_p/J_p)^{1/\dim}$ acts as a scaling term for the deformation gradient used for constitutive update.

In FEM, for which the $\bar{\mathbf{F}}$ method was originally proposed, \bar{J}_p can be calculated straightforwardly as the average of J_p in each element. In MPM, however, such element/cell-wise averaging is not ideal, because the basis functions are often related to adjacent elements to avoid cell-crossing errors (e.g. GIMP and B-splines). As such, when Coombs *et al.* [14] applied the $\bar{\mathbf{F}}$ method to GIMP, they had to introduce an additional basis function specialized to element-wise averaging. Unfortunately, introducing such a special basis function is not only cumbersome but also restricted to a specific MPM scheme. For example, the formulation in Coombs *et al.* [14] is not compatible with other MPM basis functions.

3.2. Volume averaging

In this work, we present a new approach to volume-averaging J_p in MPM, which builds on the existing particle–grid transfer schemes and hence preserves the existing basis functions. Concretely, it first projects the Jacobians at the particles to the background grid in a volume-averaging

manner, in a way similar to the P2G transfer. Then, through the G2P transfer, the volume-averaged Jacobians at the nodes are mapped back to the particles, so that they can be used for constitutive updates at the individual particles.

To express the approach mathematically, let us define the volume-averaged projection of J_p to the background grid, as

$$\bar{J}_i = \sum_p w_{ip} J_p V_p / V_i, \quad V_i := \sum_p w_{ip} V_p. \quad (19)$$

It can be seen that this projection is more or less the same as the standard P2G transfer, except that the particle volume is considered for volume averaging. Next, we project back \bar{J}_i —the volume-averaged Jacobian defined at the grid nodes—to the particles where \bar{F} is used for updating the stress tensor. For this purpose, we use the standard G2P transfer as

$$\bar{J}_p = \sum_i w_{ip} \bar{J}_i. \quad (20)$$

For notational simplicity in the succeeding formulations, we shall express the foregoing operation as the operator $\Pi(\circ)$, say,

$$\Pi(J_p) := \bar{J}_p = \sum_i w_{ip} \bar{J}_i. \quad (21)$$

Remark 1. While the projection-based averaging described above appears similar to that in Telikicherla and Moutsanidis [21], there are a couple of critical differences. First, the projection operation in Telikicherla and Moutsanidis [21] utilizes lower-order basis functions than their basis functions (B-splines) for other parts of MPM. For this reason, their projection entails an additional background mesh dedicated to the projection. Second, their methods applies the projection to the divergences of the velocity and stress fields in the variational equation, while we apply the projection to the Jacobian before stress update.

Remark 2. The foregoing volume-averaging operation is analogous to the projection scheme utilized for mitigating locking in a different meshfree method in Ortiz-Bernardin *et al.* [34], where the authors adapted the assumed deformation gradient operation in Brocardo *et al.* [35] to the meshfree context. It is noted, however, that the formulation of Ortiz-Bernardin *et al.* [34] involves a modification of the strain–displacement matrix in addition to the volume-averaging projection. This is different from the approach proposed herein, whereby the volume-averaging operation is used to evaluate \bar{F} only and the existing discretization is retained.

Remark 3. Unlike the existing \bar{F} MPM formulations where the volume averaging of J is performed inside individual cells [14–16], here the volume averaging is done inside the support of the basis functions associated with individual particles. This way allows us to accommodate particles that

influence multiple cells without any change in the existing basis functions. When an implicit integration is used, however, it may be less desirable than introducing a new basis function, because it would be more onerous to calculate the derivative of $\bar{\mathbf{F}}$. For an explicit integration—dominant in the MPM community—the projection operation must be far simpler than modifying the basis functions.

3.3. Stress update procedure

We now discuss how to update the stress tensor of a material point with the proposed approach. Consider the stress update stage during an MPM update between t^n (previous time step) and t^{n+1} (next time step). All the quantities of the particle at t^n , including the assumed deformation gradient, $\bar{\mathbf{F}}_p^n$, are known. However, the quantities at t^{n+1} are unknown, except the deformation gradient, \mathbf{F}_p^{n+1} , calculated from Eq. (14).

Let us recall that the stress update is based on the relative deformation gradient, Eq. (16). Since we use the $\bar{\mathbf{F}}$ method, we define the *relative* $\bar{\mathbf{F}}$ as

$$\Delta\bar{\mathbf{F}}_p := \bar{\mathbf{F}}_p^{n+1} \cdot (\bar{\mathbf{F}}_p^n)^{-1}. \quad (22)$$

It is noted that while the (original) deformation gradient at t^{n+1} , \mathbf{F}_p^{n+1} , is given from the updated velocity, the assumed deformation gradient at t^{n+1} , $\bar{\mathbf{F}}_p^{n+1}$, is not given directly. So we first derive the following expression for $\bar{\mathbf{F}}_p^{n+1}$:

$$\begin{aligned} \bar{\mathbf{F}}_p^{n+1} &= \left(\frac{\bar{J}_p^{n+1}}{J_p^{n+1}} \right)^{1/\dim} \mathbf{F}_p^{n+1} \\ &= \left(\frac{\bar{J}_p^{n+1}}{J_p^n \Delta J_p} \right)^{1/\dim} \mathbf{F}_p^{n+1} \\ &= \left(\frac{\bar{J}_p^{n+1} \bar{J}_p^n}{J_p^n \bar{J}_p^n \Delta J_p} \right)^{1/\dim} \mathbf{F}_p^{n+1} \\ &= \left(\frac{\bar{J}_p^{n+1}}{\bar{J}_p^n \Delta J_p} \right)^{1/\dim} \Delta \mathbf{F}_p \cdot \mathbf{F}_p^n \left(\frac{\bar{J}_p^n}{J_p^n} \right)^{1/\dim} \\ &= \left(\frac{\bar{J}_p^{n+1}}{\bar{J}_p^n \Delta J_p} \right)^{1/\dim} \Delta \mathbf{F}_p \cdot \bar{\mathbf{F}}_p^n \end{aligned} \quad (23)$$

where

$$\Delta J_p := \det(\Delta \mathbf{F}_p), \quad \bar{J}_p^n := \det(\bar{\mathbf{F}}_p^n), \quad J_p^n := \det(\mathbf{F}_p^n). \quad (24)$$

Equation (23) has replaced \mathbf{F}_p^{n+1} by the product of $\Delta \mathbf{F}_p$, which is given in the G2P stage as in Eq. (16), and $\bar{\mathbf{F}}_p^n$, which was used for evaluating the stress tensor at t^n . In doing so, it has also

replaced J_p^{n+1} in the denominator of the scaling term by $\bar{J}_p^n \Delta J_p$. Inserting Eq. (23) into Eq. (22) gives

$$\begin{aligned}\Delta \bar{\mathbf{F}}_p &= \left(\frac{\bar{J}_p^{n+1}}{\bar{J}_p^n \Delta J_p} \right)^{1/\dim} \Delta \mathbf{F}_p \cdot \bar{\mathbf{F}}_p^n \cdot (\bar{\mathbf{F}}_p^n)^{-1} \\ &= \left(\frac{\bar{J}_p^{n+1}}{\bar{J}_p^n \Delta J_p} \right)^{1/\dim} \Delta \mathbf{F}_p.\end{aligned}\quad (25)$$

Comparing the above equation with Eq. (18), one can see that the above equation is an incremental version of the $\bar{\mathbf{F}}$ method. The final task is to evaluate \bar{J}_p^{n+1} as a volume-averaged version of the term in the denominator of the scaling term. To this end, we apply the volume-averaging operator proposed earlier, $\Pi(\circ)$, as

$$\bar{J}_p^{n+1} = \Pi(\bar{J}_p^n \Delta J_p). \quad (26)$$

Substituting Eq. (26) into Eq. (25) gives

$$\Delta \bar{\mathbf{F}}_p = \left(\frac{\Pi(\bar{J}_p^n \Delta J_p)}{\bar{J}_p^n \Delta J_p} \right)^{1/\dim} \Delta \mathbf{F}_p. \quad (27)$$

Algorithm 1 presents a detailed stress-update procedure in which the proposed locking-mitigation approach is applied. We emphasize that the proposed approach only modifies the stress update during the G2P stage, preserving all the other aspects described in Section 2. For example, the particle volume update, Eq. (15), remains unchanged.

4. Numerical examples

In this section, we verify and demonstrate the performance of the proposed locking-mitigation approach through four numerical examples involving various types of nearly incompressible materials. The first example is Cook’s membrane [36], which is a popular benchmark problem for incompressible elasticity. The second example is the problem of a strip footing on an incompressible elastoplastic solid, for which an analytical solution (the Prandtl solution) is available for the bearing capacity. The third example is the dam break problem in Mast *et al.* [8], where a nearly incompressible fluid (water) is allowed to flow freely. The fourth and last example is a 3D landslide problem in which undrained clay—an elastoplastic and incompressible solid—collapses. Except for the last 3D example, plane-strain conditions are considered. Gravity is neglected in the first and second examples.

To confirm that the proposed approach works well regardless of the MPM basis functions, we simulate each example with two different basis functions, namely, GIMP and B-splines. The specific GIMP scheme used herein is uGIMP [37] in which the influence domains of individual

Algorithm 1 Stress update procedure with the proposed locking-mitigation approach

1. Calculate the (original) relative deformation gradient:

$$\Delta \mathbf{F}_p = \mathbf{1} + \Delta t \sum_i \mathbf{v}_i^{n+1} \otimes \nabla w_{ip}.$$

2. Compute $\Delta J_p = \det(\Delta \mathbf{F}_p)$ and $\bar{J}_p^n = \det(\bar{\mathbf{F}}_p^n)$.
3. Calculate volume-averaged Jacobians at nodes:

$$\bar{J}_i^{n+1} = \sum_p w_{ip} V_p^n (\bar{J}_p^n \Delta J_p) / V_i^n, \quad V_i^n = \sum_p w_{ip} V_p^n.$$

4. Compute the relative assumed deformation gradient:

$$\begin{aligned} \Delta \bar{\mathbf{F}}_p &= \left(\frac{\Pi(\bar{J}_p^n \Delta J_p)}{\bar{J}_p^n \Delta J_p} \right)^{1/\dim} \Delta \mathbf{F}_p \\ &= \left(\frac{\sum_i w_{ip} \bar{J}_i^{n+1}}{\bar{J}_p^n \Delta J_p} \right)^{1/\dim} \Delta \mathbf{F}_p. \end{aligned}$$

5. Update the particle stress with the relative assumed deformation gradient, $\Delta \bar{\mathbf{F}}_p$.
-

particles are fixed. The particular B-splines used in the following results are quadratic B-splines. While not presented for brevity, we have also found that the proposed method manifests similar performance when cubic B-splines are used. The MPM results in this section are produced using the Taichi library [38].

4.1. Cook's membrane

To verify our formulation in a simple setting, we first simulate Cook's membrane problem [36], which has widely been used as a benchmark problem for incompressible elasticity. As shown in Fig. 2, this problem considers a trapezoidal membrane subjected to a distributed shear traction on its right side and clamped on its left side. To compare our $\bar{\mathbf{F}}$ -MPM results with those of $\bar{\mathbf{B}}$ -MPM results in Bisht *et al.* [19], we set the shear load and material parameters identical to those in the reference paper. The load is set as 1 N. The membrane is a Neo-Hookean solid with a Young's modulus of $E = 70$ Pa and a Poisson's ratio of $\nu = 0.499$ (nearly incompressible).

To examine the convergence of the numerical solutions, we use two levels of spatial discretization: (i) a coarse discretization that uses 5,776 material points with a background grid comprised of 1-m-long square elements, and (ii) a fine discretization that uses 23,072 material points with

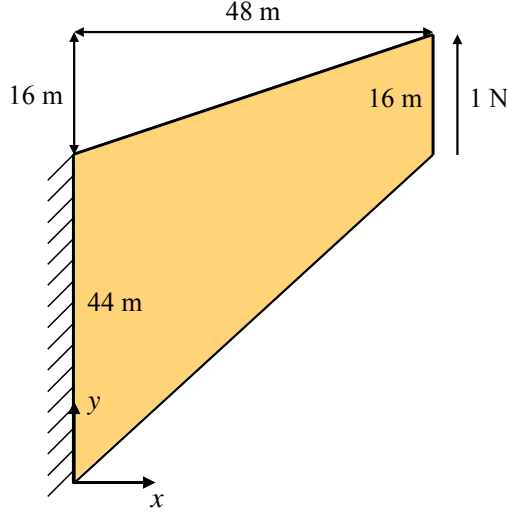


Figure 2: Cook’s membrane: problem geometry and boundary conditions.

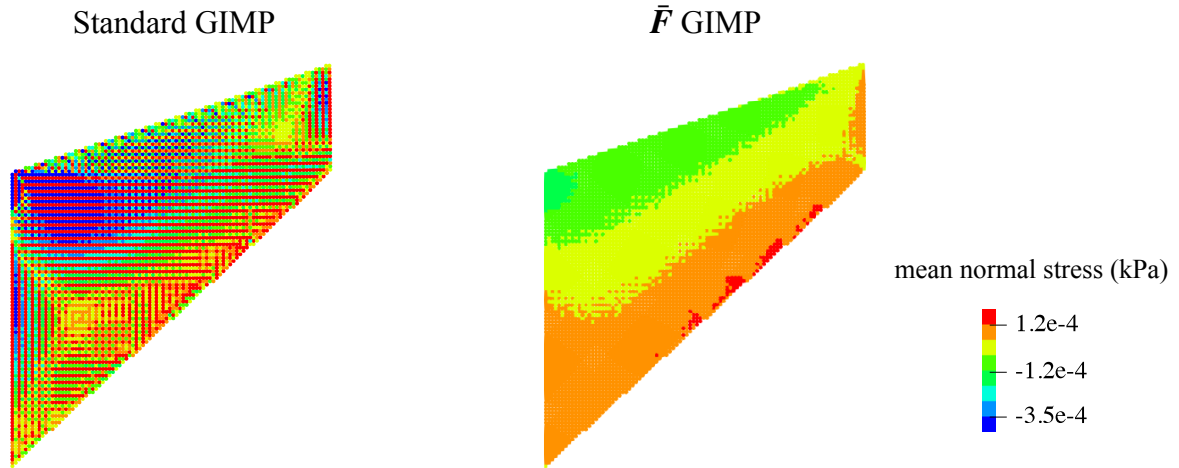
a background grid comprised of 0.5-m-long square elements. To simulate this quasi-static problem with the current explicit dynamic formulation, we adopt the local damping method in Al-Kafaji [39], with the same local damping factor used in Bisht *et al.* [19]. We calculate the time increment as $\Delta t = 0.3(h/c)$, where h is the element size and c is the P-wave velocity. This calculation gives $\Delta t = 2.773 \times 10^{-3}$ s for the coarse grid and $\Delta t = 1.386 \times 10^{-3}$ s for the fine grid.

Figure 3 presents the mean normal stress fields obtained by the standard and \bar{F} MPM formulations with GIMP. As can be seen, the standard MPM solutions are plagued by severe non-physical stress oscillations, which are not remedied by spatial refinement. Such oscillations have been commonly observed in numerical solutions affected by volumetric locking. Meanwhile, the \bar{F} MPM solutions are free of non-physical oscillations in the stress fields. This difference indicates that the proposed formulation does not suffer from volumetric locking.

Figure 4 shows how the mean normal stress fields become different when the basis functions are changed to B-splines. One can see that the B-spline MPM provides less oscillatory stress fields than GIMP, especially when the discretization is fine. Still, however, the standard MPM solutions show undesirable oscillations. Meanwhile, the same \bar{F} MPM formulation continues to work well notwithstanding the change in the basis functions.

For further verification, we compare our GIMP solution with the reference solution from Bisht *et al.* [19]—obtained with a nonlinear \bar{B} method specialized to GIMP—in terms of the mean normal stress field and the vertical displacement at the tip (upper right corner), respectively, in Figs. 5 and 6. From Fig. 5, we can see that the mean normal stress fields in the two solutions are very similar. Figure 6 also shows that the tip displacements in the \bar{F} and \bar{B} solutions are very close, while those in the standard MPM solutions are noticeably lower than the locking-free solutions. It would be worthwhile to note that the nonlinear \bar{B} MPM solution itself has also been verified with

(a) Coarse discretization (5,776 material points)



(b) Fine discretization (23,072 material points)

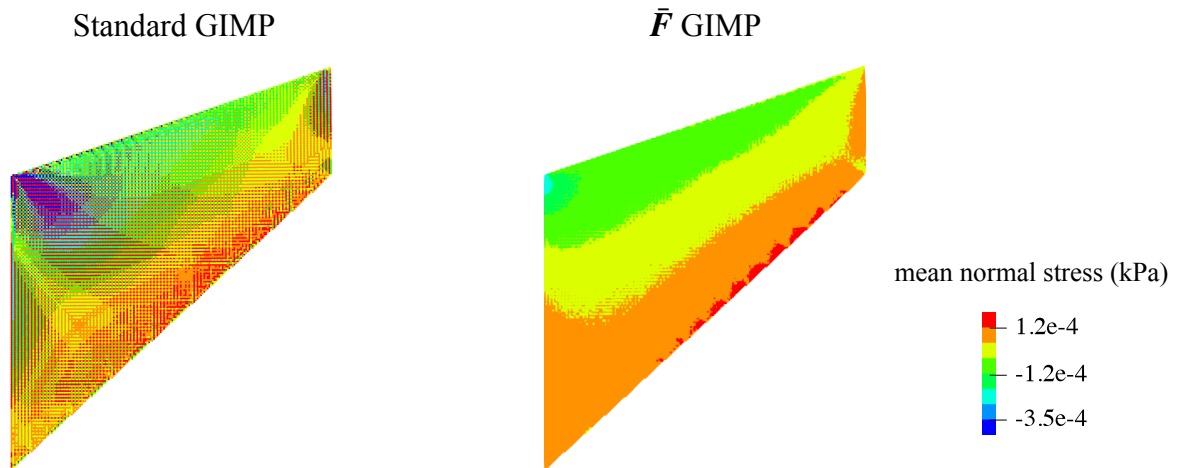
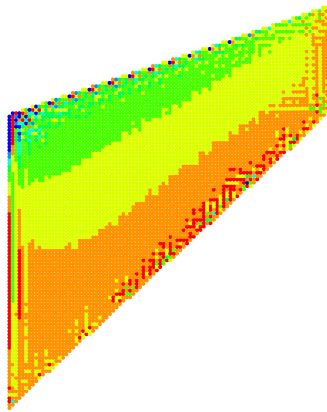


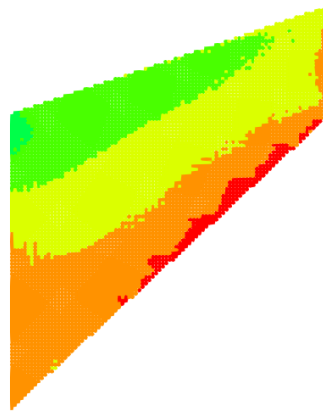
Figure 3: Cook's membrane: mean normal stress fields in the standard and \bar{F} MPM solutions, obtained with GIMP basis functions.

(a) Coarse discretization (5,776 material points)

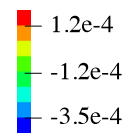
Standard B-splines



\bar{F} B-splines

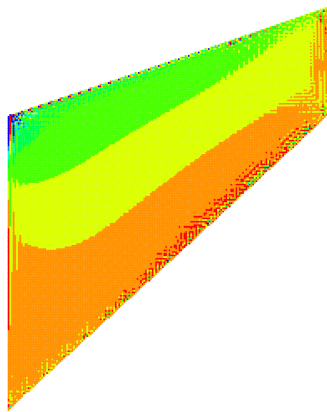


mean normal stress (kPa)

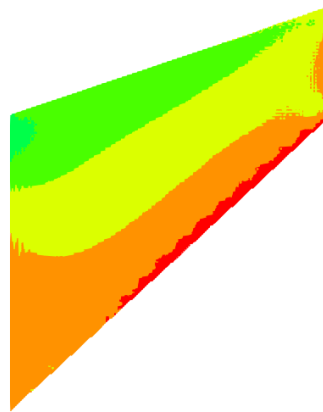


(b) Fine discretization (23,072 material points)

Standard B-splines



\bar{F} B-splines



mean normal stress (kPa)

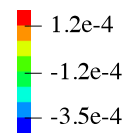


Figure 4: Cook's membrane: mean normal stress fields in the standard and \bar{F} MPM solutions, obtained with B-splines basis functions.

other results in the literature, see Bisht *et al.* [19] for more details. Taken together, it has been confirmed that the proposed method performs similarly to the nonlinear $\bar{\mathbf{B}}$ method.

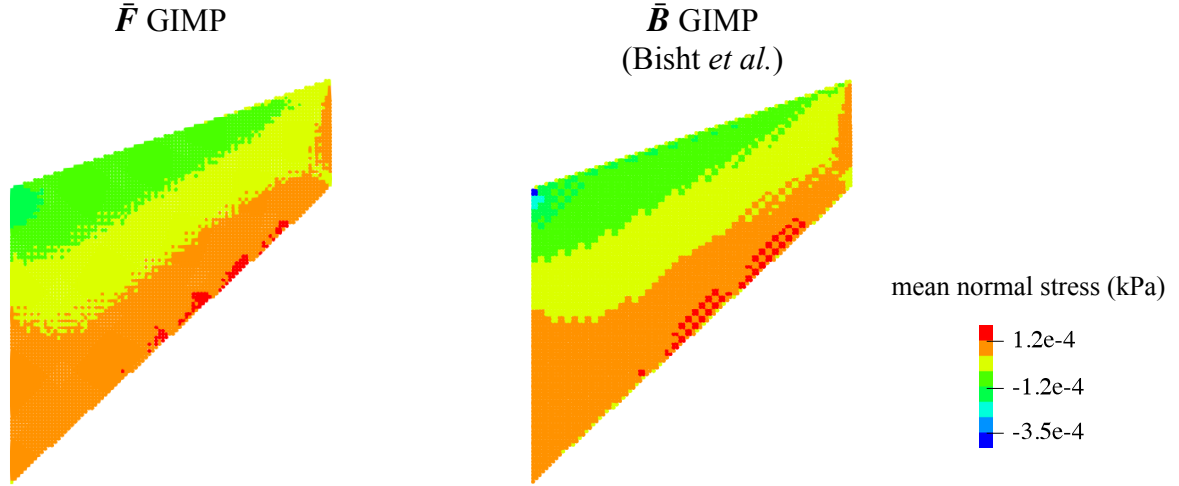


Figure 5: Cook's membrane: comparison of our $\bar{\mathbf{F}}$ GIMP solution with the $\bar{\mathbf{B}}$ GIMP solution in Bisht *et al.* [19]. Both solutions are produced with 5,776 material points.

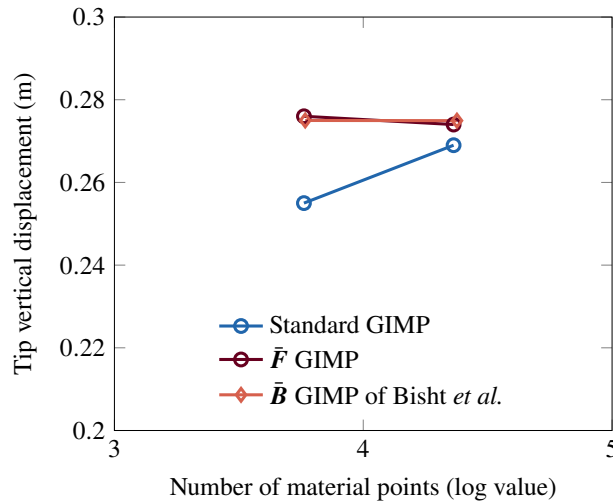


Figure 6: Cook's membrane: tip vertical displacements in our $\bar{\mathbf{F}}$ GIMP solution and the $\bar{\mathbf{B}}$ GIMP solution in Bisht *et al.* [19].

4.2. Strip footing

In our second example, we investigate the performance of the proposed approach when a nearly incompressible material is in contact with a rigid body—a common scenario in many engineering applications. To this end, we simulate the problem of a strip footing on an incompressible elastoplastic solid, for which an analytical solution for the bearing capacity—the Prandtl solution—is

available. Figure 7 depicts the specific geometry and boundary conditions simulated herein. As shown in the figure, only the right half of the problem is modeled taking advantage of symmetry. Note that the footing is treated explicitly as a rigid body.

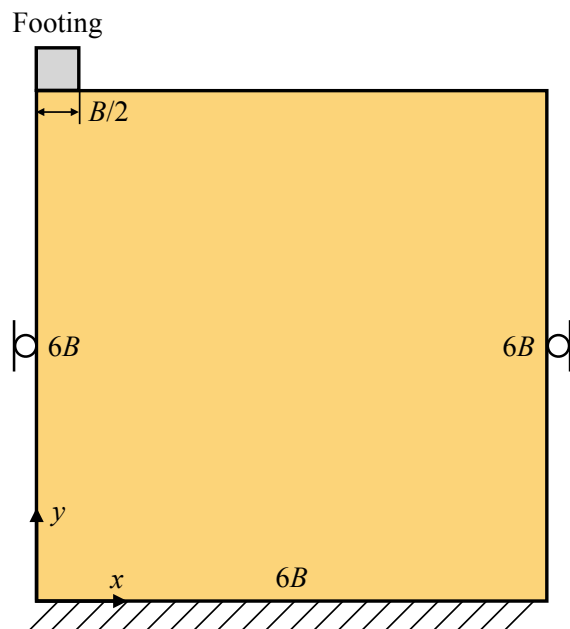


Figure 7: Strip footing: problem geometry and boundary conditions. B refers to the width of the footing.

We treat the contact between the footing and the ground with a barrier method [40–43], which guarantees non-interpenetration between the two objects. The particular barrier method implemented in this example is based on the formulation specialized to MPM [43]. The friction coefficient in the contact model is set to be sufficiently large to prevent slip between the footing and the ground.

The elastoplastic behavior of the ground is described by a combination of Hencky elasticity and J2 plasticity. The elasticity parameters assigned are a Young’s modulus of $E = 1000$ kPa and a Poisson’s ratio $\nu = 0.49$. The yield strength of J2 plasticity is set such that the (undrained) shear strength of the ground is 0.1 kPa under plane strain. These parameters are adopted from Bisht *et al.* [19]. Note that the high ratio between the Young’s modulus and the shear strength allows the ground to be in the small deformation range, such that the bearing capacity can be estimated by Prandtl’s analytical solution.

Similar to the previous example, we investigate the performance of the proposed approach under three different levels of discretization. They are: (i) $h = B/20$ (57,600 material points), (ii) $h = B/40$ (230,400 material points), and (iii) $h = B/80$ (921,600 material points). The time increment is calculated as $\Delta t = 0.4(h/c)$, which gives $\Delta t = 1.529 \times 10^{-4}$ s, $\Delta t = 7.644 \times 10^{-5}$ s, and $\Delta t = 3.822 \times 10^{-5}$ s, respectively, for the three levels of grid sizes. To emulate a quasi-static

condition, we apply the damping method used in the previous example (with a damping coefficient of 0.002), as well as pushing the footing slowly with the same penetration rate used in Bisht *et al.* [19].

Figure 8 presents the normalized load–displacement curves produced from the standard and \bar{F} MPM, along with the analytical solution, 5.14. (The load is normalized by the shear strength, and the displacement is normalized by the footing width.) As is well known, the standard MPM significantly overestimates the bearing capacity due to volumetric locking. One can see that the proposed method well remedies the problem regardless of the basis functions used, giving numerical solutions converging to the analytical solution.

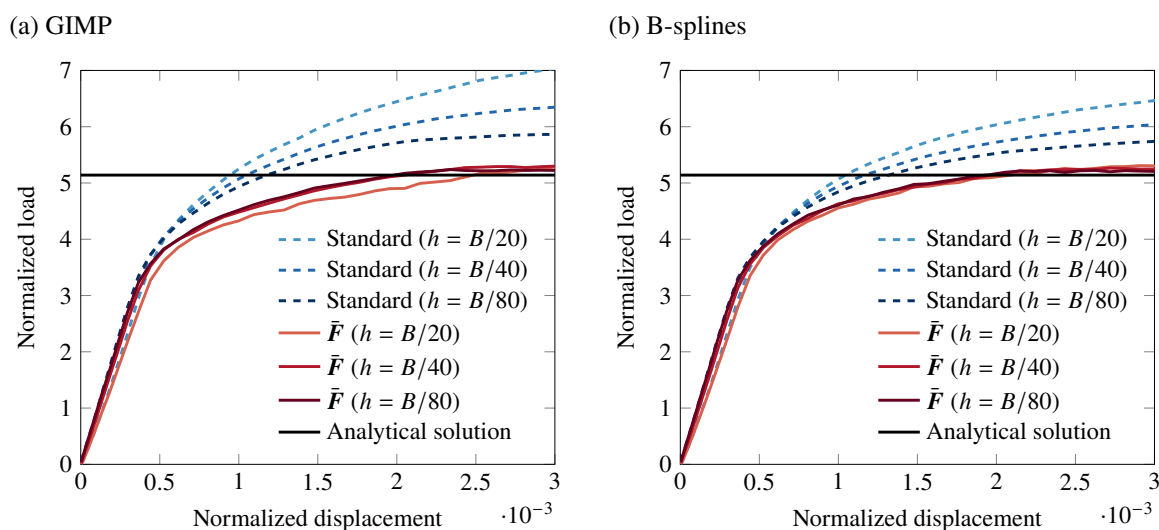


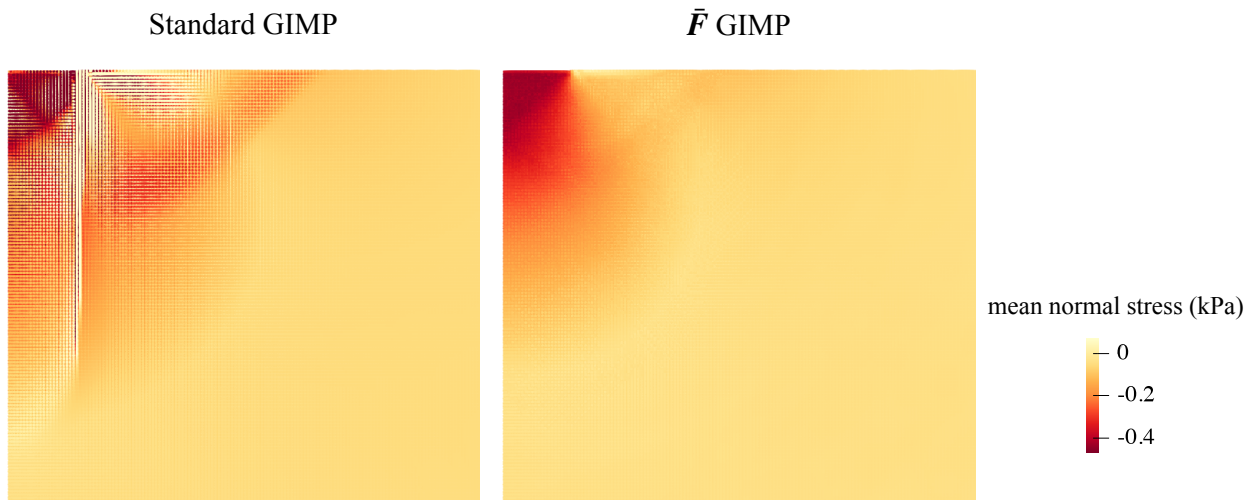
Figure 8: Strip footing: normalized load–displacement curves from the standard and \bar{F} MPM solutions, obtained with GIMP and B-splines basis functions.

Figure 9 shows the mean normal stress fields in the standard and \bar{F} MPM solutions, when $h = B/40$. As in Cook’s membrane example, the standard MPM solutions show non-physical oscillations in the stress fields, which are particularly severe when GIMP is used. The solutions obtained by the proposed \bar{F} MPM, however, are free of such oscillations. Taking this result together with the bearing capacity results above, it can be concluded that the proposed method successfully alleviates volumetric locking in MPM where contact is involved.

4.3. Dam break

Our third example is the dam break problem in Mast *et al.* [8], where a three-field mixed formulation is used for mitigating locking in MPM. Figure 10 depicts the geometry and boundary conditions of the problem. As shown, it considers a 4-m-long and 2-m-high water reservoir that is initially constrained by a gate and starts to flow after the gate is removed. It is noted that there is another gate on the right boundary, from which the water will bounce back.

(a) GIMP



(b) B-splines

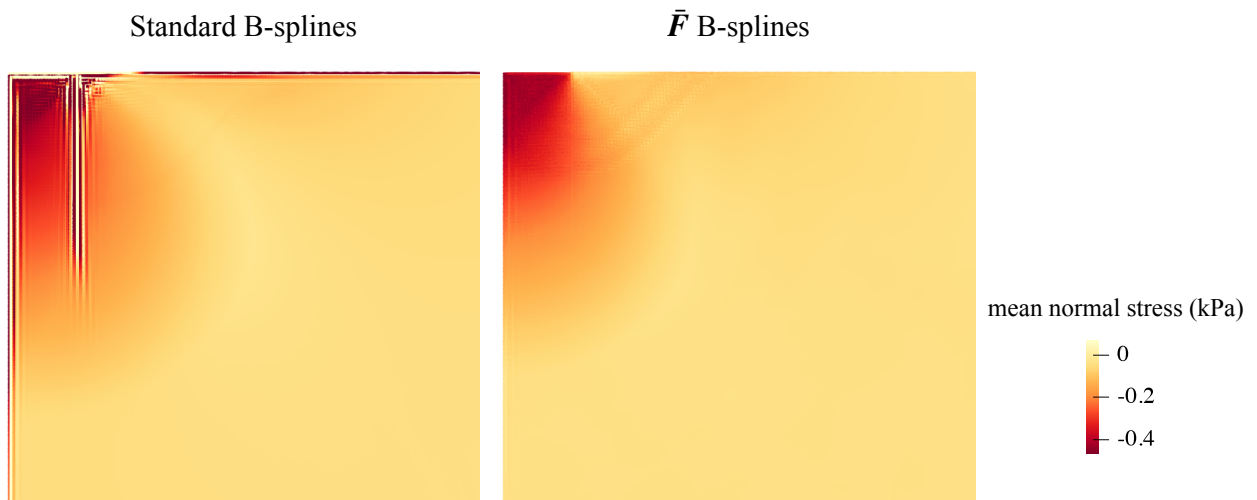


Figure 9: Strip footing: mean normal stress fields in the standard and \bar{F} MPM solutions, obtained with GIMP and B-splines basis functions.

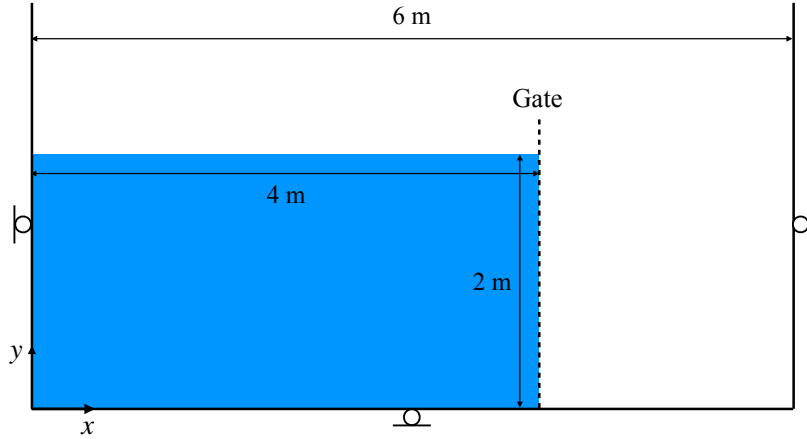


Figure 10: Dam break: problem geometry and boundary conditions.

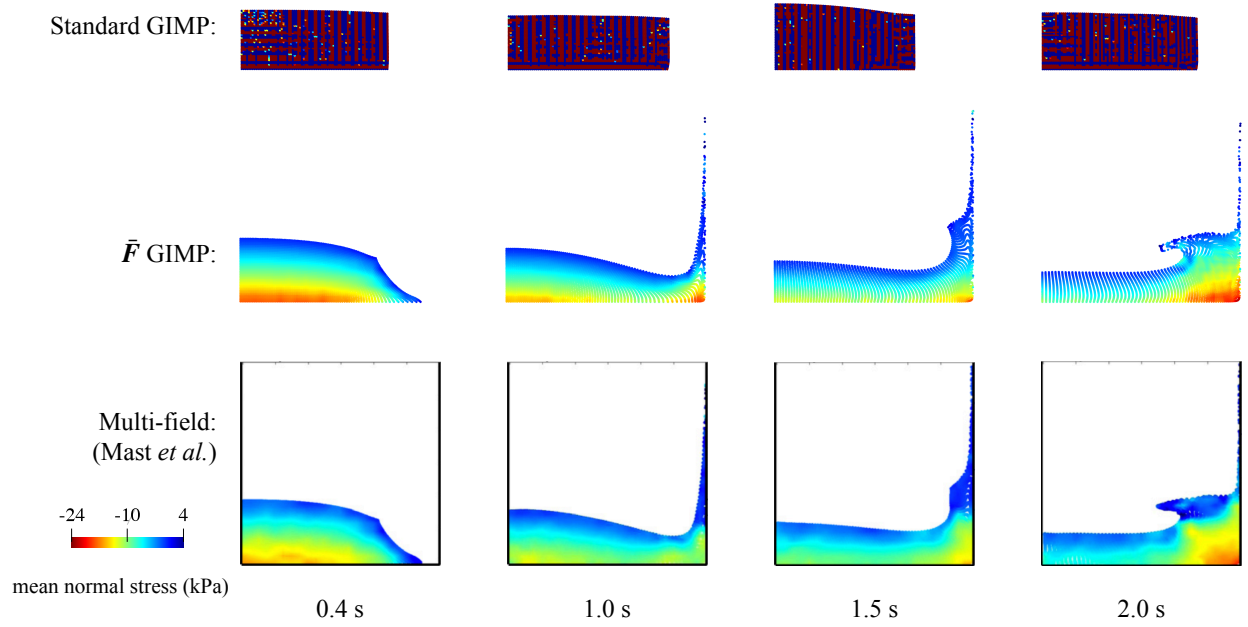
Following Mast *et al.* [8], the water is modeled as a nearly incompressible Newtonian fluid, with a bulk modulus of $K = 2.0$ GPa, a dynamic viscosity of $\mu = 0.001$ Pa·s, and a density of $\rho = 0.9975$ t/m³. For MPM discretization, we introduce a background grid comprised of 0.25-m long square elements and initialize each element with 25 material points. This results in 3,200 material points in total. We then apply gravity loading to the water reservoir until it reaches the hydrostatic state. Subsequently, we remove the gate so that the water can flow freely. We simulate the problem until $t = 2.0$ s, setting the time increment as $\Delta t = 10^{-5}$ s.

Figure 11 shows the flow snapshots simulated by the standard and \bar{F} MPM formulations (with both GIMP and B-splines), in comparison with the reference solutions from Mast *et al.* [8]. One can easily see that the standard MPM is subjected to severe volumetric locking. Not only does the pressure field show non-physical oscillations, but the water also is unrealistically stiff. The locking is less severe in B-splines MPM than GIMP, but it is still unacceptable. When the \bar{F} MPM formulation is employed, however, the numerical solutions are free of the locking problem, irrespective of the basis functions. It can also be seen that the numerical solutions produced by the \bar{F} MPM formulation are very similar to those by the three-field mixed MPM formulation [8]. It is reminded that the proposed method involves significantly less implementation effort and computational cost than the three-field mixed formulation.

4.4. 3D landslide

As our last example, we investigate the performance of the proposed approach for 3D large deformation in an elastoplastic material. To this end, we simulate a 3D landslide process where a brittle clay slope fails in an undrained manner. The slope geometry is depicted in Fig. 12. The bottom boundary of the slope is fully fixed, while the three lateral boundaries are supported by rollers. The elastoplastic behavior of the undrained clay is modeled through a combination of Hencky elasticity and J2 plasticity with a softening law. The specific softening law adopted is

(a) GIMP



(b) B-splines

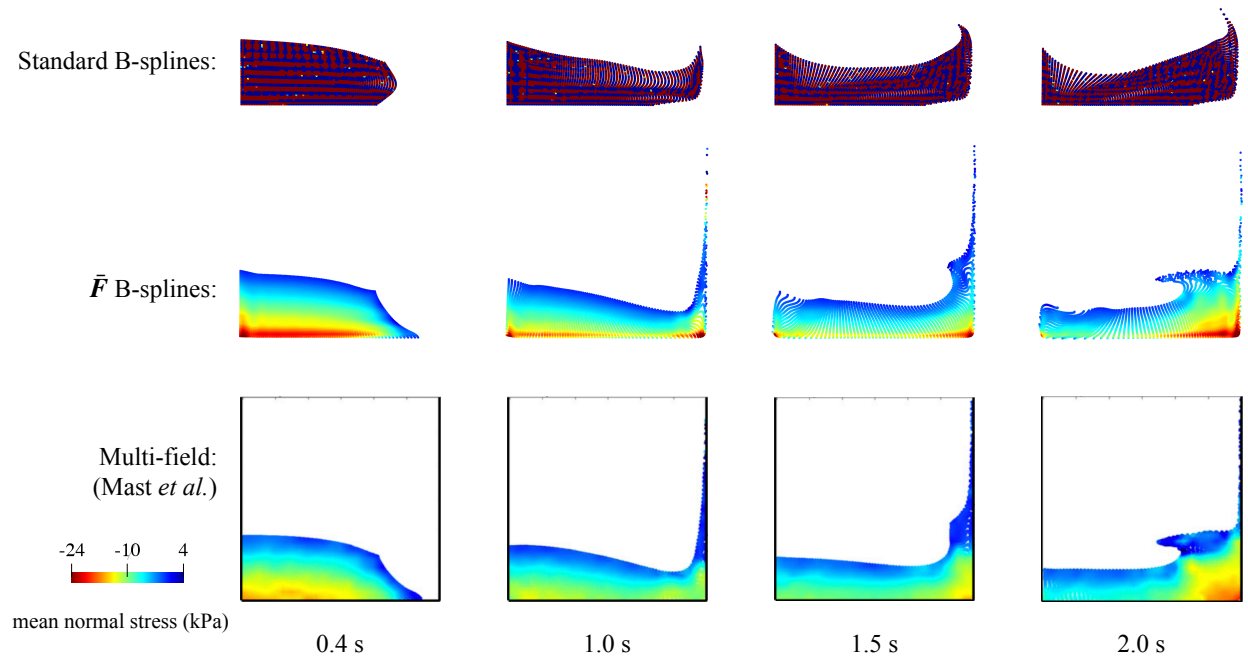


Figure 11: Dam break: flow snapshots from the standard and \bar{F} MPM simulations, along with those from Mast *et al.* [8] produced from a three-field mixed MPM formulation. Material points are colored by the water pressure.

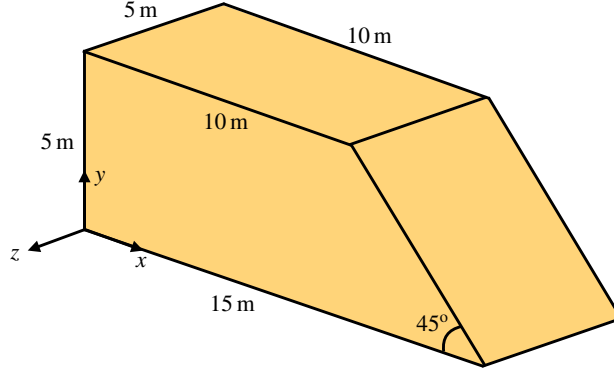


Figure 12: 3D landslide: problem geometry.

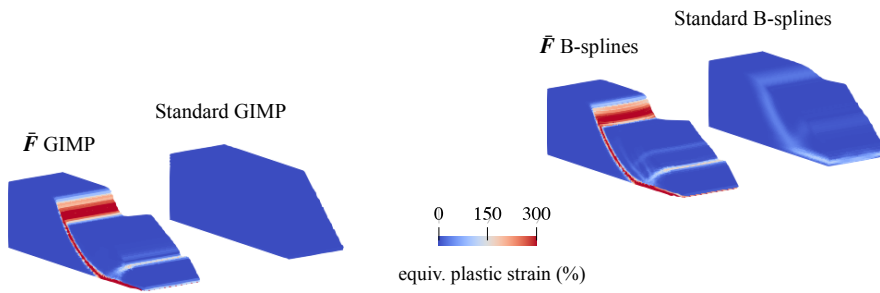
$\kappa = \kappa_r + (\kappa_p - \kappa_r)e^{-\eta\varepsilon_q^p}$, where κ is the yield strength, κ_r and κ_p are the residual and peak strengths, respectively, η is the softening parameter, and ε_q^p is the cumulative equivalent plastic strain. The material parameters are assigned to be similar to the undrained sensitive clay modeled in Bui and Nguyen [44]. They are: Young's modulus $E = 25$ MPa, Poisson's ratio $\nu = 0.499$, peak strength $\kappa_p = 40.82$ kPa, residual strength $\kappa_r = 2.45$ kPa, softening coefficient $\eta = 5$, and the density $\rho = 2.15$ t/m³.

For MPM discretization, we introduce a 3D background grid comprised of mono-sized cubic elements whose length is 0.2 m. For each element in the slope domain, we assign 8 material points, which results in a total of 311,250 material points. We initialize the stress field in the material points through a gravity loading stage. Then, to trigger the slope failure, we decrease the peak strength with a reduction factor of 1.65, as done in Bui and Nguyen [44]. We simulate the problem until 5.5 s with a time increment of $\Delta t = 5 \times 10^{-5}$ s.

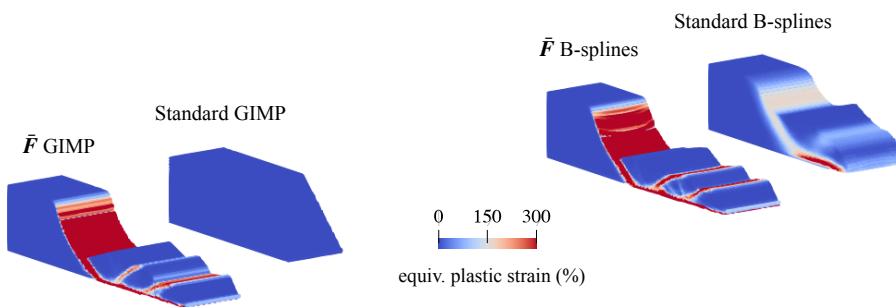
Figures 13 and 14 present snapshots of the landslide simulated by the standard and \bar{F} MPM, showing the equivalent plastic strain and mean normal stress fields, respectively. As in the previous example, the standard MPM is subjected to severe volumetric locking, manifesting non-physical stress oscillations as well as overly stiff behavior. The slope does not even fail when GIMP is used, while it shows diffusive plastic strains when B-splines are used. However, the \bar{F} MPM results show retrogressive failure—a signature failure pattern in sensitive clay slopes—with both GIMP and B-splines. Although there is no reference solution for this problem, it can be seen that the simulation results produced with the two types of basis functions are quite similar. Thus the \bar{F} MPM solutions are believed to be reasonable.

Figure 15 demonstrates how the run-out distance, which is of primary interest in slope analysis, is different in the standard and \bar{F} MPM solutions. Without a proper locking-mitigation approach, the standard MPM significantly underestimates the run-out distance, if not being unable to simulate the failure process at all. This difference highlights why it is of critical importance to mitigate volumetric locking from the practical viewpoint.

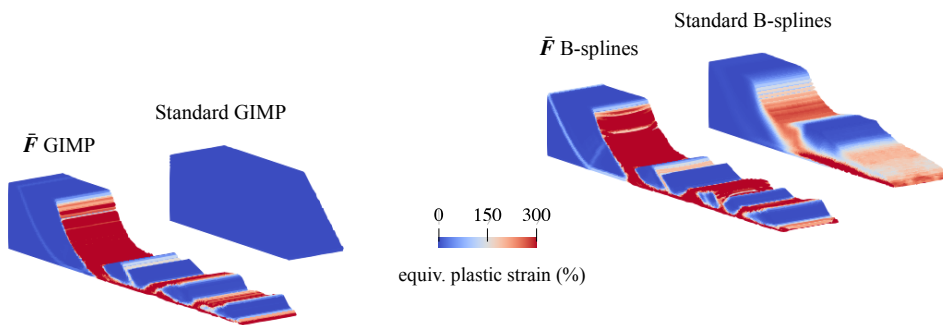
(a) $t = 1.5$ s



(b) $t = 2.5$ s



(c) $t = 3.5$ s



(d) $t = 5.5$ s

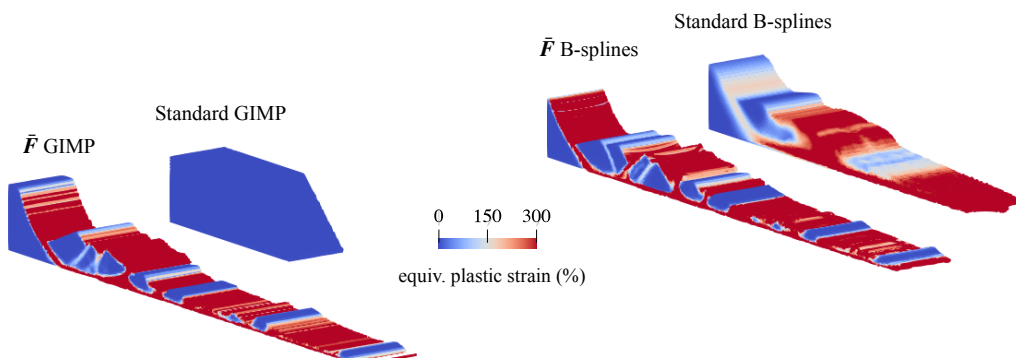
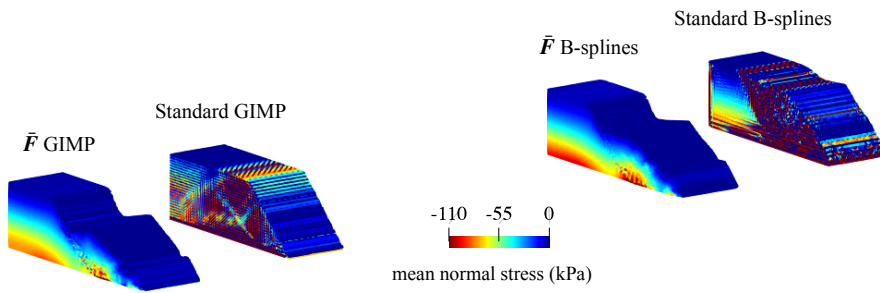
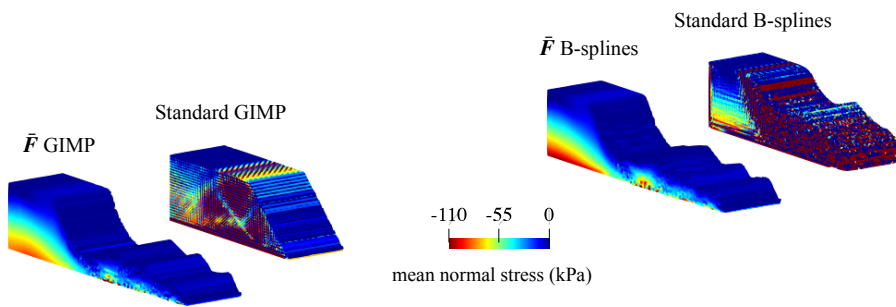


Figure 13: 3D landslides: snapshots from the standard and \bar{F} MPM simulations. Material points are colored by the equivalent plastic strain.

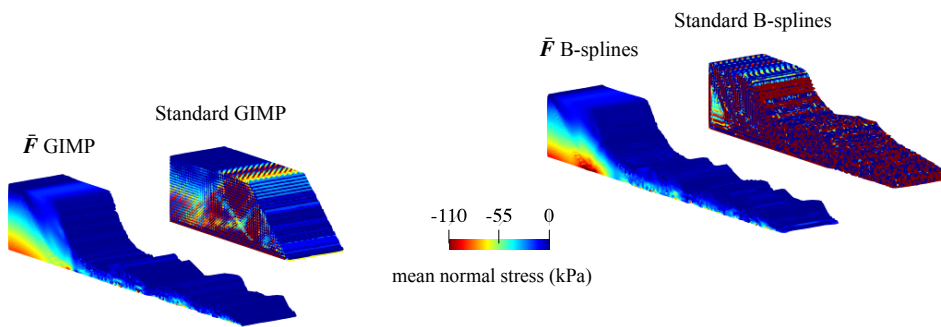
(a) $t = 1.5$ s



(b) $t = 2.5$ s



(c) $t = 3.5$ s



(d) $t = 5.5$ s

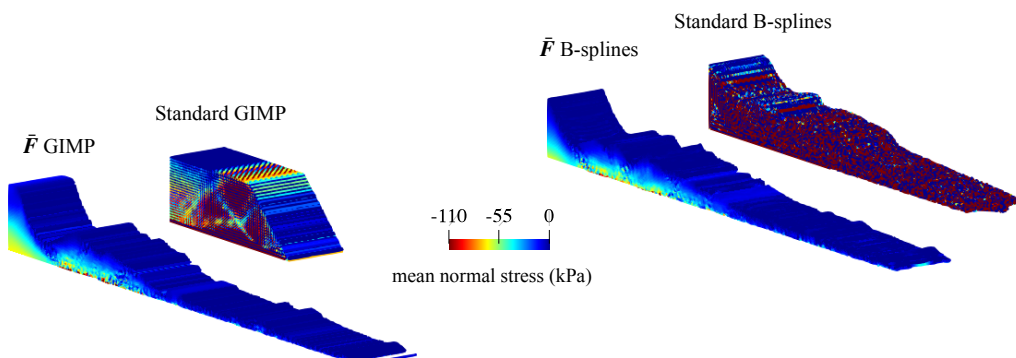


Figure 14: 3D landslides: snapshots from the standard and \bar{F} MPM simulations. Material points are colored by the mean normal stress.

(a) GIMP

0 150 300
equiv. plastic strain (%)

\bar{F} GIMP:



Standard GIMP:



(b) B-splines

0 150 300
equiv. plastic strain (%)

\bar{F} B-splines:



Standard B-splines:

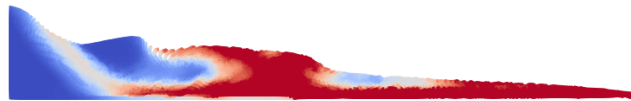


Figure 15: 3D landslides: comparison of run-out distances in the standard and \bar{F} MPM simulations.

5. Closure

In this paper, we have proposed a simple and efficient approach for circumventing volumetric locking in MPM, which can be generally applied to a family of standard explicit MPM formulations regardless of basis functions and material types. The key idea of the proposed approach is to evaluate the assumed deformation gradient (\bar{F}) with a volume-averaging operation that resembles the standard particle–grid transfer schemes in MPM. The approach can be implemented in a far simpler way than the existing approaches for mitigating locking in MPM, and it is independent of other parts such as the basis function and the constitutive behavior. The results of the numerical examples have verified and demonstrated that the proposed approach performs well for various types of nearly incompressible problems arising in solid and fluid mechanics. Taken together, it is believed that the proposed approach features unparalleled attractiveness for mitigating volumetric locking in explicit MPM.

Acknowledgments

This work was supported by the National Research Foundation of Korea (NRF) grant funded by the Korean government (MSIT) (No. 2022R1F1A1065418). The authors also wish to thank Dr. Vibhav Bisht for sharing his numerical solution to Cook’s membrane problem obtained with the nonlinear \bar{B} MPM.

Data Availability Statement

The data that support the findings of this study are available from the corresponding author upon reasonable request.

References

- [1] D. Sulsky, Z. Chen, H. L. Schreyer, A particle method for history-dependent materials, *Computer methods in applied mechanics and engineering* 118 (1-2) (1994) 179–196.
- [2] J. U. Brackbill, H. M. Ruppel, FLIP: A method for adaptively zoned, particle-in-cell calculations of fluid flows in two dimensions, *Journal of Computational Physics* 65 (2) (1986) 314–343.
- [3] J. Gaume, T. Gast, J. Teran, A. Van Herwijnen, C. Jiang, Dynamic anticrack propagation in snow, *Nature communications* 9 (1) (2018) 1–10.
- [4] J. Fern, A. Rohe, K. Soga, E. Alonso, *The Material Point Method for Geotechnical Engineering: A Practical Guide*, CRC Press, 2019.
- [5] Y. Zhao, J. Choo, Stabilized material point methods for coupled large deformation and fluid flow in porous materials, *Computer Methods in Applied Mechanics and Engineering* 362 (2020) 112742.
- [6] X. Li, B. Sovilla, C. Jiang, J. Gaume, Three-dimensional and real-scale modeling of flow regimes in dense snow avalanches, *Landslides* (2021) 1–14.
- [7] E. Love, D. L. Sulsky, An energy-consistent material-point method for dynamic finite deformation plasticity, *International Journal for Numerical Methods in Engineering* 65 (10) (2006) 1608–1638.

- [8] C. Mast, P. Mackenzie-Helnwein, P. Arduino, G. R. Miller, W. Shin, Mitigating kinematic locking in the material point method, *Journal of Computational Physics* 231 (16) (2012) 5351–5373.
- [9] I. Iaconeta, A. Larese, R. Rossi, E. Oñate, A stabilized mixed implicit material point method for non-linear incompressible solid mechanics, *Computational Mechanics* 63 (6) (2019) 1243–1260.
- [10] F. Zhang, X. Zhang, K. Y. Sze, Y. Lian, Y. Liu, Incompressible material point method for free surface flow, *Journal of Computational Physics* 330 (2017) 92–110.
- [11] S. Kularathna, K. Soga, Implicit formulation of material point method for analysis of incompressible materials, *Computer Methods in Applied Mechanics and Engineering* 313 (2017) 673–686.
- [12] A. J. Chorin, Numerical solution of the navier-stokes equations, *Mathematics of Computation* 22 (104) (1968) 745–762.
- [13] E. de Souza Neto, D. Perić, M. Dutko, D. Owen, Design of simple low order finite elements for large strain analysis of nearly incompressible solids, *International Journal of Solids and Structures* 33 (20-22) (1996) 3277–3296.
- [14] W. M. Coombs, T. J. Charlton, M. Cortis, C. E. Augarde, Overcoming volumetric locking in material point methods, *Computer Methods in Applied Mechanics and Engineering* 333 (2018) 1–21.
- [15] L. Wang, W. M. Coombs, C. E. Augarde, M. Cortis, M. J. Brown, A. J. Brennan, J. A. Knappett, C. Davidson, D. Richards, D. J. White, et al., An efficient and locking-free material point method for three-dimensional analysis with simplex elements, *International Journal for Numerical Methods in Engineering* (2021).
- [16] G. Moutsanidis, J. J. Koester, M. R. Tupek, J.-S. Chen, Y. Bazilevs, Treatment of near-incompressibility in meshfree and immersed-particle methods, *Computational Particle Mechanics* 7 (2) (2020) 309–327.
- [17] J. Simo, R. L. Taylor, K. Pister, Variational and projection methods for the volume constraint in finite deformation elasto-plasticity, *Computer methods in applied mechanics and engineering* 51 (1-3) (1985) 177–208.
- [18] T. J. Hughes, Generalization of selective integration procedures to anisotropic and nonlinear media, *International Journal for Numerical Methods in Engineering* 15 (9) (1980) 1413–1418.
- [19] V. Bisht, R. Salgado, M. Prezzi, Simulating penetration problems in incompressible materials using the material point method, *Computers and Geotechnics* 133 (2021) 103593.
- [20] V. Bisht, R. Salgado, M. Prezzi, Material point method for cone penetration in clays, *Journal of Geotechnical and Geoenvironmental Engineering* 147 (12) (2021) 04021158.
- [21] R. M. Telikicherla, G. Moutsanidis, Treatment of near-incompressibility and volumetric locking in higher order material point methods, *Computer Methods in Applied Mechanics and Engineering* 395 (2022) 114985.
- [22] M. Steffen, R. M. Kirby, M. Berzins, Analysis and reduction of quadrature errors in the material point method (MPM), *International Journal for Numerical Methods in Engineering* 76 (6) (2008) 922–948.
- [23] Y. Gan, Z. Sun, Z. Chen, X. Zhang, Y. Liu, Enhancement of the material point method using B-spline basis functions, *International Journal for numerical methods in engineering* 113 (3) (2018) 411–431.
- [24] C. Jiang, C. Schroeder, J. Teran, A. Stomakhin, A. Selle, The material point method for simulating continuum materials, in: *ACM SIGGRAPH 2016 Courses*, 2016, pp. 1–52.
- [25] X. Zhang, Z. Chen, Y. Liu, *The Material Point Method: A Continuum-Based Particle Method for Extreme Loading Cases*, Academic Press, 2016.
- [26] A. de Vaucorbeil, V. P. Nguyen, S. Sinaie, J. Y. Wu, Material point method after 25 years: Theory, implementation, and applications, *Advances in applied mechanics* 53 (2020) 185–398.
- [27] G. A. Holzapfel, *Nonlinear solid mechanics: a continuum approach for engineering science*, *Meccanica* 37 (4) (2002) 489–490.
- [28] E. A. de Souza Neto, D. Peric, D. R. Owen, *Computational methods for plasticity: theory and applications*, John Wiley & Sons, 2011.
- [29] R. I. Borja, *Plasticity: Modeling & Computation*, Springer, 2013.

- [30] S. G. Bardenhagen, E. M. Kober, The generalized interpolation material point method, *Computer Modeling in Engineering and Sciences* 5 (6) (2004) 477–496.
- [31] F. H. Harlow, The particle-in-cell computing method for fluid dynamics, *Methods in Computational Physics* 3 (1964) 319–343.
- [32] A. de Vaucorbeil, V. P. Nguyen, C. R. Hutchinson, A Total-Lagrangian Material Point Method for solid mechanics problems involving large deformations, *Computer Methods in Applied Mechanics and Engineering* 360 (2020) 112783.
- [33] A. de Vaucorbeil, V. P. Nguyen, Modelling contacts with a total lagrangian material point method, *Computer Methods in Applied Mechanics and Engineering* 373 (2021) 113503.
- [34] A. Ortiz-Bernardin, M. Puso, N. Sukumar, Improved robustness for nearly-incompressible large deformation meshfree simulations on Delaunay tessellations, *Computer Methods in Applied Mechanics and Engineering* 293 (2015) 348–374.
- [35] M. Brocardo, M. Micheloni, P. Krysl, Assumed-deformation gradient finite elements with nodal integration for nearly incompressible large deformation analysis, *International journal for numerical methods in engineering* 78 (9) (2009) 1113–1134.
- [36] R. D. Cook, Improved two-dimensional finite element, *Journal of the Structural Division* 100 (9) (1974) 1851–1863.
- [37] P. C. Wallstedt, J. Guilkey, An evaluation of explicit time integration schemes for use with the generalized interpolation material point method, *Journal of Computational Physics* 227 (22) (2008) 9628–9642.
- [38] Y. Hu, T.-M. Li, L. Anderson, J. Ragan-Kelley, F. Durand, Taichi: a language for high-performance computation on spatially sparse data structures, *ACM Transactions on Graphics (TOG)* 38 (6) (2019) 201.
- [39] I. K. Al-Kafaji, Formulation of a dynamic material point method (MPM) for geomechanical problems, 2013.
- [40] M. Li, Z. Ferguson, T. Schneider, T. R. Langlois, D. Zorin, D. Panozzo, C. Jiang, D. M. Kaufman, Incremental potential contact: intersection-and inversion-free, large-deformation dynamics., *ACM Trans. Graph.* 39 (4) (2020) 49.
- [41] Y. Zhao, J. Choo, Y. Jiang, M. Li, C. Jiang, K. Soga, A barrier method for frictional contact on embedded interfaces, *Computer Methods in Applied Mechanics and Engineering* 393 (2022) 114820.
- [42] X. Li, Y. Fang, M. Li, C. Jiang, BFEMP: Interpenetration-free MPM–FEM coupling with barrier contact, *Computer Methods in Applied Mechanics and Engineering* 390 (2022) 114350.
- [43] Y. Jiang, Y. Zhao, C. E. Choi, J. Choo, Hybrid continuum–discrete simulation of granular impact dynamics, *Acta Geotechnica* (2022). [doi:10.1007/s11440-022-01598-2](https://doi.org/10.1007/s11440-022-01598-2).
- [44] H. H. Bui, G. D. Nguyen, Smoothed particle hydrodynamics (SPH) and its applications in geomechanics: From solid fracture to granular behaviour and multiphase flows in porous media, *Computers and Geotechnics* 138 (2021) 104315.